Version of Record: https://www.sciencedirect.com/science/article/pii/S0167278919303963
Manuscript_52b3eadd82c00718e03426b6e5d6bab2

High Speed PLIF Study of the Richtmyer-Meshkov Instability Upon Re-Shock

Christopher D. Noble*, Josh M. Herzog, Alex M. Ames, Jason Oakley, David A. Rothamer, Riccardo Bonazza

Department of Engineering Physics, University of Wisconsin - Madison, Madison, WI 53706 USA

Abstract

The Richtmyer-Meshkov instability (RMI) of a twice-shocked gas interface is studied using high-speed planar-laser induced fluorescence (PLIF) in the Wisconsin Shock Tube Laboratory's vertical shock tube. The initial condition (IC) is a shear layer with broadband diffuse perturbations at the interface between a helium-acetone mixture and argon. This IC is accelerated by a shock of nominal strength $M = 1.8$, and then accelerated again by the transmitted shock that reflects off the end wall of the tube. An estimate of the light gas mole fraction is extracted from high-speed imaging using an iterative process that accounts for the nonlinear temperature dependence of the acetone's fluorescence quantum yield (FQY) and absorption cross-section. A vorticity deposition model for the initial growth rate after re-shock is compared with the Mikaelian model for re-shock. Previously used in literature, the number of generations is shown to naturally arise from a normalisation of the scalar transport equation. A self-similar analysis is then performed using the mole fraction data to explore the evolution of the RMI after reshock and the higher order moments of the light gas mole fraction are compared with a proposed model.

Keywords: Richtmyer-Meshkov instability, High-speed imaging, PLIF
2019 MSC: 00-01, 99-00

1. Introduction

The RMI occurs when fluid layers are impulsively accelerated in a direction normal to the interfaces between the layers, leading to the growth of any perturbations. The RMI is seen as a primary cause of inefficiency in attempts to produce energy via inertial confinement fusion (ICF) [1]. The capsule and fuel form a material interface, and the process of compression with intense x-ray laser light, generated through reflection of UV laser beams off the walls of a hohlraum, causes the propagation of a shock across this boundary, leading to the mixing of the fuel and capsule material and reducing yield. The instability has also been proposed as an important mechanism by which the mixing of fuel and oxidant in hypersonic aero-engines can be increased [2].

*Corresponding author, email address: cdnoble@wisc.edu

The study of the RMI often involves the use of a shock wave in a shock tube. This is the setting originally used by Meshkov [3] to experimentally confirm Richtmyer's theory [4]. Previous studies of the RMI have used various initial conditions including: nitro-cellulose membranes [5] that provide a repeatable interface geometry and allow for gravitationally unstable configurations to be investigated; membrane-free interfaces including vertical gas curtains [6]; gravitationally stable horizontal interfaces perturbed using oscillations of the entire shock tube [7]; pistons [8]; loudspeakers [9]; transverse gas injection [10]; and precisely orientable shock tubes that can be rotated to a desired angle from vertical [11].

Previous studies have used a variety of different diagnostics for quantifying the RMI development, including: schlieren [5], particle image velocimetry (PIV) [12], correlation image velocimetry (CIV) [13] and planar laser-induced fluorescence (PLIF) [14]. A recent investigation

has combined multiple techniques with high-speed imaging [15, 16, 17]. A comprehensive review of the state of the art is presented by Zhou [18, 19].

2. Experiment Set-up

Experiments are conducted in a 9.1 m long, vertical, downward-firing shock tube with a square internal cross-section (25.4 cm on a side) shown in Fig. 1. The facility is described in detail by Anderson *et al* [20]. The 2-m long driver is filled with nitrogen to 80% of the rupture pressure of a 16-gauge steel diaphragm. The driven section is evacuated to 20 kPa, then a stagnation plane is formed by flowing the helium-acetone mixture downward from just below the diaphragm and flowing argon upward from just above the end wall of the shock tube.

Once the stagnation plane is formed, and the pressure in the tube is 110 kPa, the vacuum system is turned on pulling excess gas from the vacuum line shown in Fig. 1 and a shear layer is generated using two planar jets with argon injected above the stagnation plane and helium/acetone mixture below it. This configuration allows the resulting buoyancy forces to aid in development of Kelvin-Helmholtz roll ups. This initial condition has been used in previous studies in this facility [21, 22].

The pressure inside the tube is now at a steady state with excess gas being taken out at the interface by the vacuum system. This steady state is allowed to persist for 15 minutes to allow any air that was mixed in with the desired gases to be extracted from the system.

A pulse-burst laser system is used to create a pulse train of 10 ms duration at a repetition rate of 20 kHz. The system amplifies the output of an Nd:YVO_4 oscillator laser in Nd:YAG amplification stages. The fourth harmonic output at 266 nm is used in the experiments with an average energy of 30 mJ per pulse for each pulse in the burst. The pulse train is passed through a spherical lens and a cylindrical lens to create a diverging laser sheet that spans the entire width of the shock tube 1 m above the end wall of the tube. This laser sheet excites the acetone present in the light gas mixture causing it to fluoresce. A Phantom V1840 high-speed camera with a 1 μs exposure is used to capture the resulting fluorescence signal. Camera linearity was previously measured in a light-box, and the results are used to correct PLIF measurements.

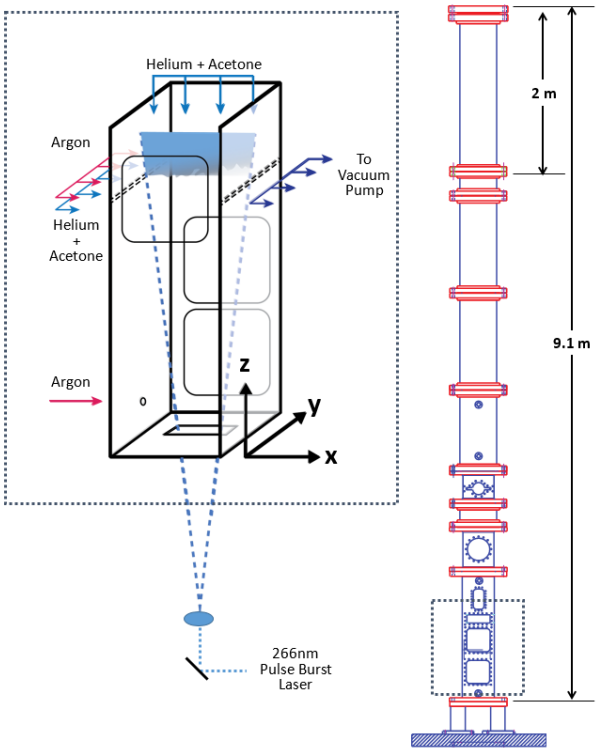

Figure 1: Diagram of test section showing coordinate system and experiment layout.

To generate a shock, the steel diaphragm is ruptured. Figure 2 shows a combined experimental and theoretical *z*-*t* diagram for HS4 (Table 1). The reference axes are oriented so that the reflected shock (green) is shown propagating in the positive *z*-direction. This reflected shock interacts with the mixing layer at time t=0; a shock is transmitted while a rarefaction is reflected which then reflects off the end wall of the shock tube and interacts with the mixing layer. This interaction causes the centroid of the mixing layer to become stationary within the field of view. At 3 ms, there is a compression wave propagating vertically downward which is the transmitted shock reflecting off the contact surface between the driver gas and the driven gas. This causes the mixing layer to begin propagating downward while also compressing the mixing layer.

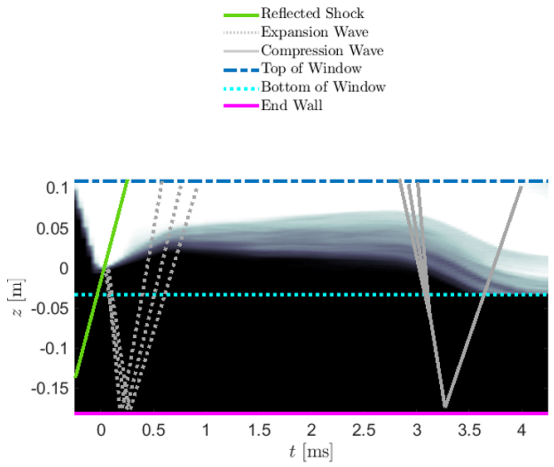

Figure 2: Combined experimental and theoretical z-t diagram showing the spanwise averaged light gas mole fraction as a function of z and t from HS4 (Table 1). $z = 0$ and $t = 0$ represent the spatial and temporal location of the interaction of the reflected shock with the interface. The overlaid wave pattern is generated from 1D gas dynamics and shows the initial shock, reflected rarefaction and a compression train from the shock reflecting off the contact surface above the window (the contact surface being the surface separating the driver gas from the driven gas.)

3. Concentration measurements from PLIF

A procedure based on the method described in [14] is used to extract an estimate of the light gas mole fraction from each frame of the captured high-speed video. The camera operation is such that 10 frames are obtained before the arrival of the interface into the field of view. These 10 frames are used to generate a background signal which is then subtracted from each frame containing the interface so that a region of zero light gas mole fraction has a signal level of zero. Each frame is then transformed into an $r-\theta$ coordinate system aligned with the laser sheet and is corrected for signal decrease due to laser sheet divergence.

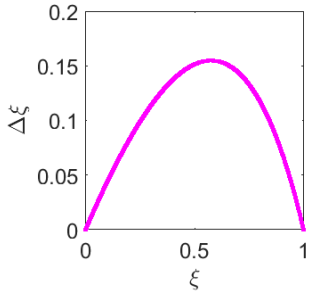

Figure 3: Absolute difference in mole fraction when using linear material property variation with temperature versus the full non-linear material properties.

Finally, the signal must be corrected along each ray to account for attenuation according to Beer's law and adiabatic mixing. The procedure is described in equations 1 and 2 and is explored in detail in [23].

$$\xi = \frac{n(r)}{n(r_0)}\frac{\overline{T}(r)}{\overline{T}(r_0)} = \frac{\overline{T}(r)}{\overline{T}(r_0)}\frac{S(r)}{S(r_0)}\frac{\Phi(r_0)}{\Phi(r)}\frac{\sigma(r_0)}{\sigma(r)}[1+ n(r_0)\sigma(r_0)\int_{r_0}^{r}\frac{S(r')}{S(r_0)}\frac{\Phi(r_0)}{\Phi(r')}dr']^{-1} \quad (1)$$

$$\overline{T} = \frac{\xi C_{p,1}(T_1)T_1 + (1-\xi)C_{p,2}(T_2)T_2}{\xi C_{p,1}(\overline{T}) + (1-\xi)C_{p,2}(\overline{T})} \quad (2)$$

Equation 1 is the resulting expression for the estimate of mole fraction, ξ, as a function of r along a light ray where n is the number density, $\overline{T}$ is the mole fraction averaged temperature, S is the background-subtracted signal, Φ is the fluorescence quantum yield, and σ is the absorption cross section. The ratio n/n_0 is well estimated by this procedure, however the light gas mole fraction is only approximately known due to the possibility of diffusion of acetone from helium to argon. Both Φ and σ depend nonlinearly on temperature. Here the model from Thurber *et al* [24] is used to calculate this behaviour. Using this, along with an ideal gas equation of state for each component, the adiabatic mixing rule, Eq. 2 in parallel with Eq. 1 is solved iteratively to find an estimate for ξ.

Figure 3 shows the difference between using a linear material property approximation *vs*. the full non-linear properties, encouraging the use of the more complex iterative algorithm for the estimation of mole fraction at re-shock temperatures and pressures for acetone PLIF.

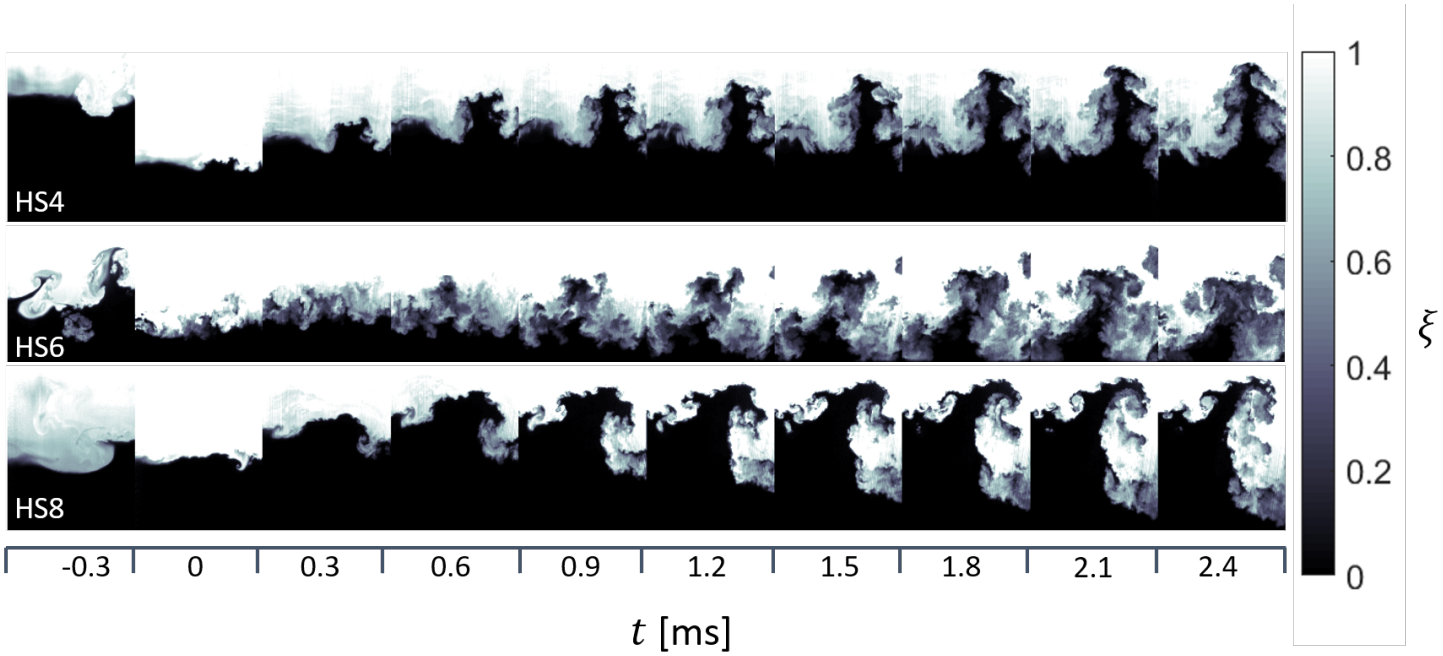

Figure 4: Example mole fraction fields evolving with time from 3 experiments. Details of each run are given in Table 1.

The bulk temperatures in gas 1 and 2 are estimated from 1D gas dynamics using wave speeds measured by the pressure transducers (PTs) along the length of the shock tube, and the interface velocity is measured using the high-speed video. The wave speed of the incident shock is well captured by the PTs with 5 PTs capturing arrival times, while the bulk velocities of the interface after shock and after re-shock are well captured by the high-speed PLIF imaging with at least 5 frames capturing the position of the interface after each wave interaction.

With the measurement of the incident wave speed and the initial bulk interface velocity, the composition and shock strength can be determined, then the bulk temperatures, pressures and densities after successive wave interactions can be estimated.

Figure 4 shows a subset of the resulting light gas mole fraction fields, each row being a time series with the first image being the re-shock initial condition, and the second image being the frame after the reflected shock has fully traversed the interface.

4. Non-Dimensionalisation of Governing Equations

4.1. Deforming Reference Frame

Here the transport equation for the light gas mole fraction is transformed into a deforming frame of reference that follows the centroid of the interface and scales with the mixing width. This has the same form as found by Ristorcelli *et al.* [25] except a change of variables in the time derivative term shows that $\ln h^*$ appears as the evolution parameter. This is to allow an identification of terms and a comparison between experiments. The functional form of this transformation is $\xi(x,z,t) \rightarrow \xi(x^*,z^*,h^*)$ with $x^* = \dfrac{x}{W}$, $z^* = \dfrac{z-z_0}{h}$ and $h^* = \dfrac{h}{h_0}$ where W is some representative spanwise length scale (here it is the shock tube width), z_0 is the time-varying location of the interface center, h is the time-varying mixing thickness and h_0 is the initial mixing thickness after re-shock.

Introducing the spanwise average in the x-direction of some function f as

$$\overline{f} = \frac{1}{W}\int_0^W f\, dx \tag{3}$$

such that $\xi = \overline{\xi} + \xi'$, the mixing thickness is defined as

$$h = 4\int_{-\infty}^{\infty} \overline{\xi}(1-\overline{\xi})\, dz. \tag{4}$$

Our data analysis starts with the transport equation for ξ

$$\frac{\partial(\xi)}{\partial t} + \boldsymbol{\nabla}\cdot\boldsymbol{u}\xi = \mathcal{D}\boldsymbol{\nabla}^2\xi, \tag{5}$$

where $\boldsymbol{u}$ and $\mathcal{D}$ are the velocity and mass diffusivity, respectively. Specialising to 2D, and introducing the following non-dimensionalisation

$$\boldsymbol{u}^* = \frac{\boldsymbol{u} - V_0\hat{e}_z}{\dot{h}} \tag{6}$$

where $V_0 = \dfrac{\partial z_0}{\partial t}$ is the bulk velocity of the interface in the lab fixed frame and $z_0 = 4\displaystyle\int_{-\infty}^{\infty} z\overline{\xi}(1-\overline{\xi})dz$ is the mixing fraction-weighted centroid. One can show (Appendix A) that Eq.5 rewrites as

$$\frac{\partial\xi}{\partial\ln h^*} - z^*\frac{\partial\xi}{\partial z^*} + \frac{\partial u^*\xi}{\partial x^*}\frac{h}{W} + \frac{\partial w^*\xi}{\partial z^*} = \frac{1}{Re_h Sc}\left[\frac{\partial^2\xi}{\partial x^{*2}}\left(\frac{h}{L}\right)^2 + \frac{\partial^2\xi}{\partial z^{*2}}\right]. \tag{7}$$

This leads to evolution equations for the mean and variance of the light gas mole fraction:

$$\frac{\partial\overline{\xi}}{\partial\ln h^*} - z^*\frac{\partial\overline{\xi}}{\partial z^*} + \frac{\partial\overline{w^*\xi'}}{\partial z^*} = \frac{1}{Re_h Sc}\frac{\partial^2\overline{\xi}}{\partial z^{*2}} \tag{8}$$

$$\frac{\partial\overline{\xi'^2}}{\partial\ln h^*} - z^*\frac{\partial\overline{\xi'^2}}{\partial z^*} + \overline{w^*\xi'}\frac{\partial\overline{\xi}}{\partial z^*} + \frac{\partial\overline{w^*\xi'^2}}{\partial z^*} = \frac{1}{Re_h Sc}\frac{\partial^2\overline{\xi'^2}}{\partial z^{*2}} - C_\chi^* \tag{9}$$

where $Re_h = \dfrac{h\dot{h}}{\nu}$, $Sc = \dfrac{\nu}{\mathcal{D}}$ and $C_\chi^* = 2\mathcal{D}\dfrac{\overline{\xi'^2}}{\lambda^2}\dfrac{h}{\dot{h}}$ with λ being the scalar Taylor micro-scale defined as $\lambda^2 = \dfrac{\overline{\xi'^2}}{\overline{\left(\dfrac{\partial\xi'}{\partial x_i}\right)^2}}$, summing over i.

The number of generations $n_g = \ln h^*$ appears here as the appropriate dimensionless time for a shock-driven mixing layer. The number of generations used in [26] is the doubling time, which is the logarithm base 2 of the normalised mixing width, however the natural logarithm here follows as a result of the normalisation. These are related by a factor of $\ln 2$.

4.2. Translating Reference Frame

If the normalizations are held constant in time such that the functional form of the transformation becomes $\xi(x,z,t) \rightarrow \xi(x^*,z^\times,\tau)$ with $x^* = \frac{x}{W}$, $z^\times = \frac{z-z_0}{h_0}$ and $\tau = t\frac{\dot{h}_0}{h_0}$ where $\dot{h}_0$ is the initial growth rate after re-shock, then the normalised equation for the mean and variance respectively become

$$\frac{\partial\bar{\xi}}{\partial\tau} + \frac{\partial\overline{w^\times\xi'}}{\partial z^\times} = \frac{1}{Re_{h0}Sc}\frac{\partial^2\bar{\xi}}{\partial z^{\times 2}} \tag{10}$$

$$\frac{\partial\overline{\xi'^2}}{\partial\tau} + \overline{w^\times\xi'}\frac{\partial\bar{\xi}}{\partial z^\times} + \frac{\partial\overline{w^\times\xi'^2}}{\partial z^\times} = \frac{1}{Re_{h0}Sc}\frac{\partial^2\overline{\xi'^2}}{\partial z^{\times 2}} - C_\chi \tag{11}$$

where $\boldsymbol{u}^\times = \frac{\boldsymbol{u} - V_0\hat{e}_z}{\dot{h}_0}$, $Re_{h0} = \frac{h_0\dot{h}_0}{\nu}$ and $C_\chi = 2\mathcal{D}\frac{\overline{\xi'^2}}{\lambda^2}\frac{h_0}{\dot{h}_0}$, where $\dot{h}_0$ is the initial growth rate of the interface after reshock and after completion of phase reversal.

5. Results and Discussion

Table 1 shows the details of each experimental run including: the incident shock strength (M_s), the post-shock (A^+) and post-re-shock (A^{++}) Atwood numbers, and the post-re-shock Reynolds number (Re_{h0}).

Figure 5 shows the plot of the initial growth rate of the interface after re-shock normalised by the jump in interface translation velocity against the theoretical value of this ratio. Two models are considered. The first is Mikaelian's

$$\frac{\dot{h}_0}{\Delta V_0} = C_M A^{++} \tag{12}$$

where ΔV_0 is the jump in interface bulk translational velocity, A^{++} is the post-re-shock Atwood number, and C_M is an empirically fitted value. C_M has been shown to have a range from 0.28 to 0.9 by Ukai *et al* [27]. Here $C_M = 0.28$ and $C_M = 0.9$ is used with $C_M = 0.28$ corresponding to the original value ascertained from RT experiments and $C_M = 0.9$ being the value found by Ukai *et al* to fit well for sharp 3D ICs. Here the ICs are diffuse and closer to 2D. The second is a vorticity deposition model furthering work by Weber [28].

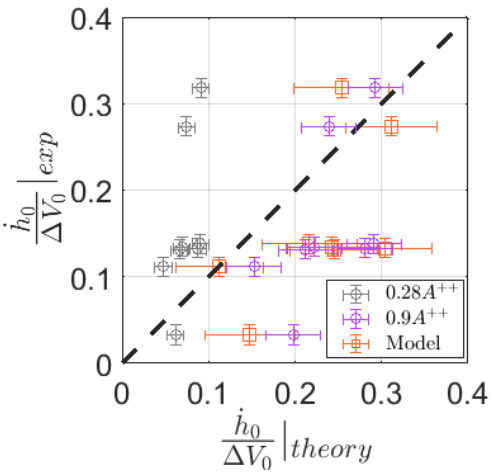

Figure 5: Plot of normalised initial growth rate of the mixing thickness directly after re-shock.

$$\frac{\dot{h}_0}{\Delta V_0} = 8\int_{-\infty}^{\infty}\overline{(\ln\rho)'\xi'}\frac{\partial\bar{\xi}}{\partial z}dz - \frac{\dot{h}_{prs}}{\Delta V_0}. \tag{13}$$

Here ρ is approximated as $\rho = \rho_0(1+(R^{++}-1)\xi)$ where ρ_0 is the density of the light gas after re-shock and R^{++} is the post-re-shock density ratio. $\dot{h}_{prs}$ is the interface growth rate before re-shock. A derivation of Eq. (13) is shown in Appendix B. This model does not use any empirical fitting constants and Fig. 5 shows a better agreement between this model and measurements than Eq. (12).

5.1. Spanwise Averaged Moments

A subset of three experiments are studied. The IC for each experiment is shown in Fig. 6. HS4 and HS8 have similar structures while HS6 has a markedly dissimilar structure. This will allow a comparison of IC influence on moment evolution.

Figure 7 shows the normalised mixing thickness against the normalised time. The dashed black line represents a linear growth rate with time. This behavior is seen initially in all three experiments with HS4 and HS8 deviating from this linear growth while HS6 persists with

	M_s	A^+	A^{++}	Re_{h0}	h_0 [cm]	$\dot{h}_0$ [m/s]	$X_{acetone}$ %
HS1	1.88	0.320	0.323	$2.6\text{x}10^4$	1.17	36.58	6.7
HS2	1.89	0.320	0.326	$2.5\text{x}10^5$	2.21	121.3	5.1
HS3	1.93	0.268	0.266	$3.0\text{x}10^5$	2.02	127.5	2.1
HS4	1.94	0.253	0.247	$4.7\text{x}10^4$	0.46	71	3.8
HS5	1.96	0.230	0.221	$1.8\text{x}10^4$	0.63	16.53	1.8
HS6	1.90	0.306	0.312	$7.8\text{x}10^4$	0.82	66	2
HS7	1.99	0.191	0.170	$2.5\text{x}10^4$	0.34	51.2	2.9
HS8	1.95	0.244	0.236	$1.9\text{x}10^4$	0.24	68.92	2.4

Table 1: Parameters of high-speed experiments

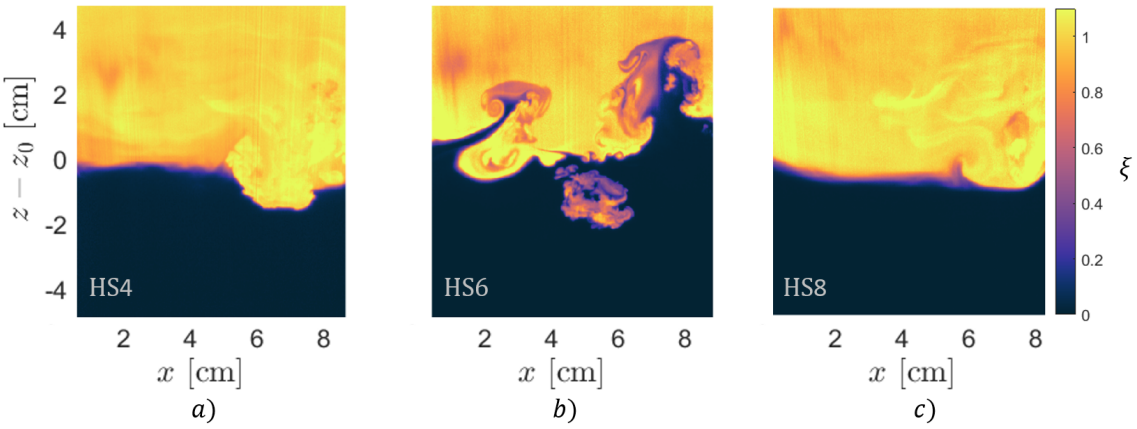

Figure 6: Light gas mole-fraction of the ICs of the three experiments analysed in further detail in section 5. a) HS4, b) HS6, c) HS8.

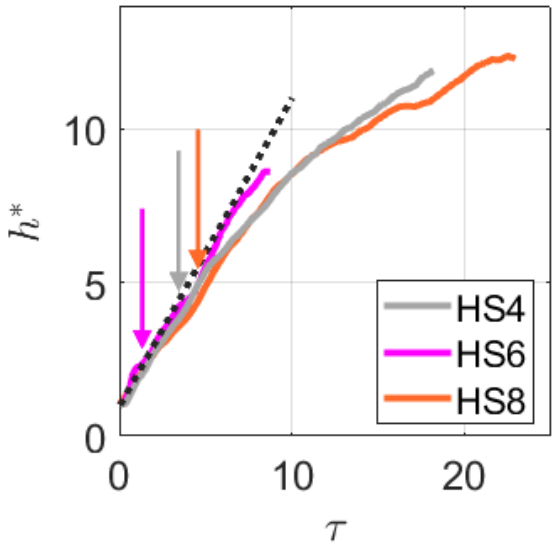

Figure 7: Plot of normalised mixing width vs normalised time. Arrows correspond to the arrival time of the 1st rarefaction wave.

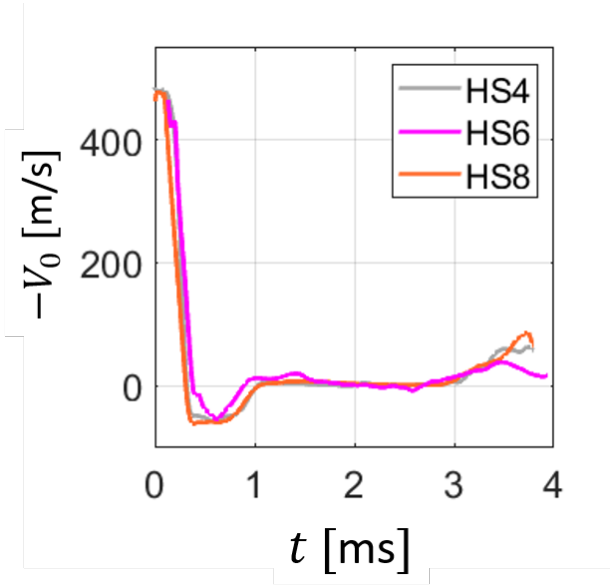

Figure 8: Downward vertical velocity of the mole fraction-weighted centroid of the mixing layer.

a linear growth until the arrival of the reflected compression wave shown in Fig. 2.

The plot of interface bulk velocity in Fig. 8 shows the forcing applied to the interface is consistent between experiments HS4, HS6 and HS8. An initial downward shocked velocity is first observed; upon reshock, the interface has an upward velocity until interaction with the rarefaction reflecting off the bottom wall of the shock tube. After 1 ms, the interface is stationary until the arrival of the compression wave (around 3 ms after the start of high speed imaging).

The structure of the ICs is plotted in Fig. 9, showing the spanwise average, spanwise variance, integrated phase spectrum and integrated energy spectrum. These may be combined to generate a model interface such that $\xi(z^*, x^*) = \overline{\xi} + \mathcal{F}_x^{-1}[\sqrt{\overline{\xi'^2}} E_\xi e^{i\Theta}]$ where $\mathcal{F}$ is the Fourier transform.

Figure 10 plots the spanwise average light gas mole fraction. The initial linear growth phase after re-shock has similar structures here between all three experiments, however, at later physical times, large variations in the structure occur that are experiment dependent.

The spanwise variance, plotted in Fig. 11, is a measure of the local departure from mixedness. All three experiments begin with a Gaussian-like profile, nearly symmetric about the center of the mixing layer. There is an initial reduction in magnitude due to phase reversal occurring where structures invert. In a single mode system this would potentially allow the variance to momentarily fall to zero. Here, in a multi-modal system, different structures will have different speeds at which they will reverse phase only reducing the variance. In HS4 and HS8, this phase reversal is followed by a growth in the extent of bulk structures, with more smaller scale mixing occurring on the heavy gas side, as seen by the lower values of the variance in the region $z^* < 0$, and with bulk penetration on the light gas side, leading to asymmetric development of the profiles. HS6 follows its phase reversal with a period of stronger mixing where the variance is much lower between $\tau = 0.5$ and $\tau = 3$. Bulk structure growth here only occurs after interaction of the rarefaction with the interface and can be seen in the profile plot of the variance as the spike at around $z^* = 0.5$. This interaction leads to growth of a bulk structure that produces similar magnitude profiles at late times though with a stronger

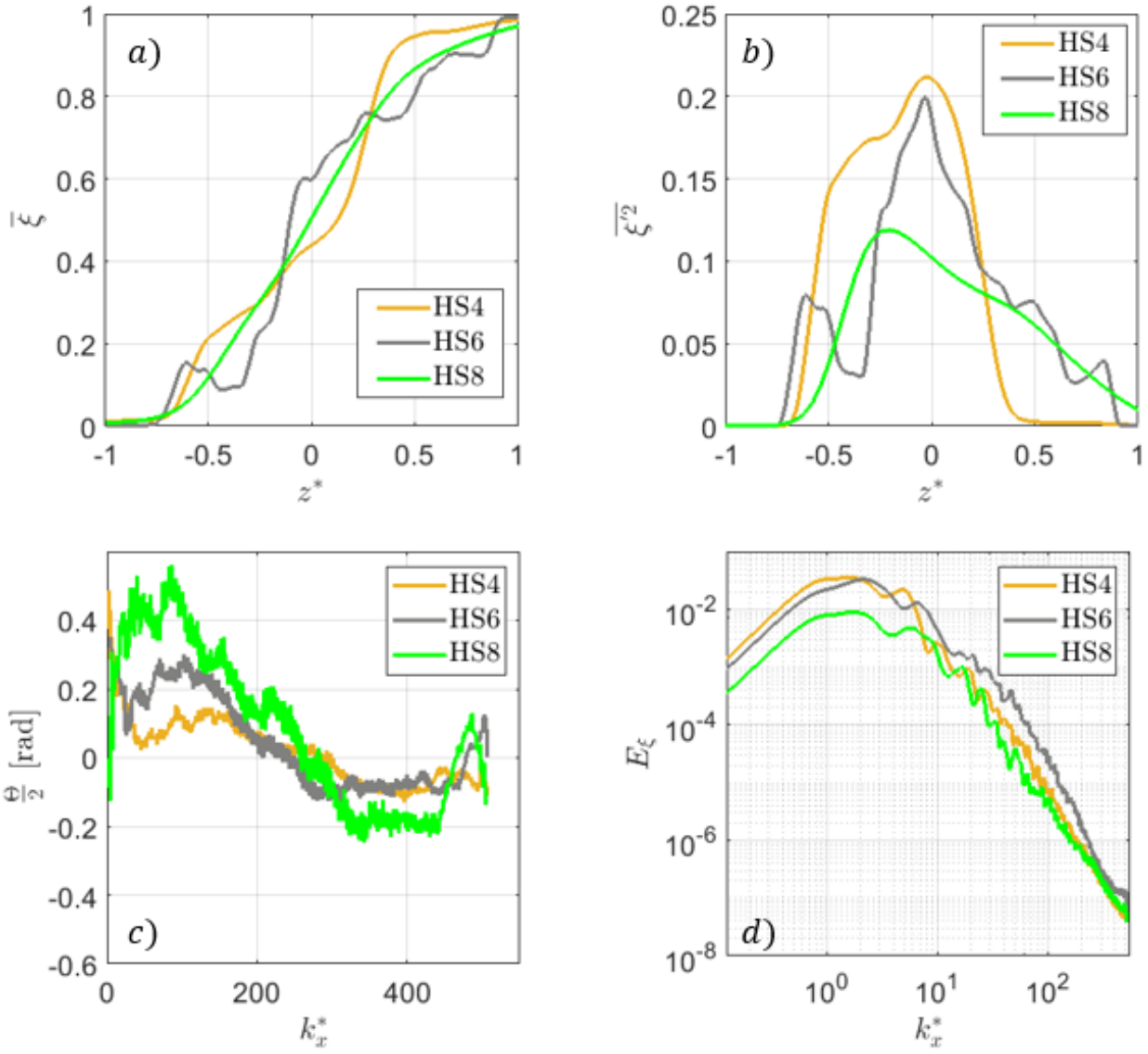

Figure 9: IC parameters. a) spanwise average light gas mole fraction, b) spanwise variance of light gas mole fraction, c) integrated phase spectrum, d) integrated power spectrum.

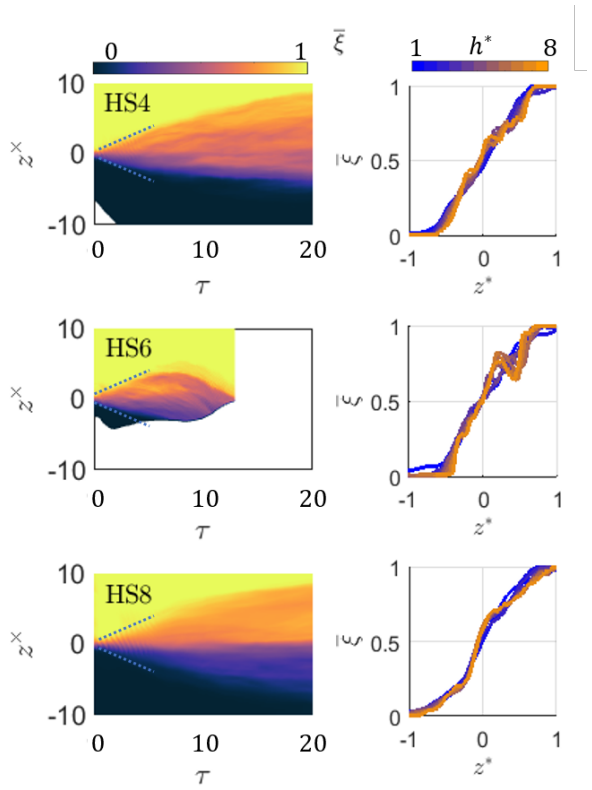

Figure 10: Left: contour plot of the spanwise averaged light gas mole fraction $\overline{\xi}$ in translating reference frame. Right: profiles of $\overline{\xi}$ in the deforming reference frame. (Dotted lines: linear growth trend)

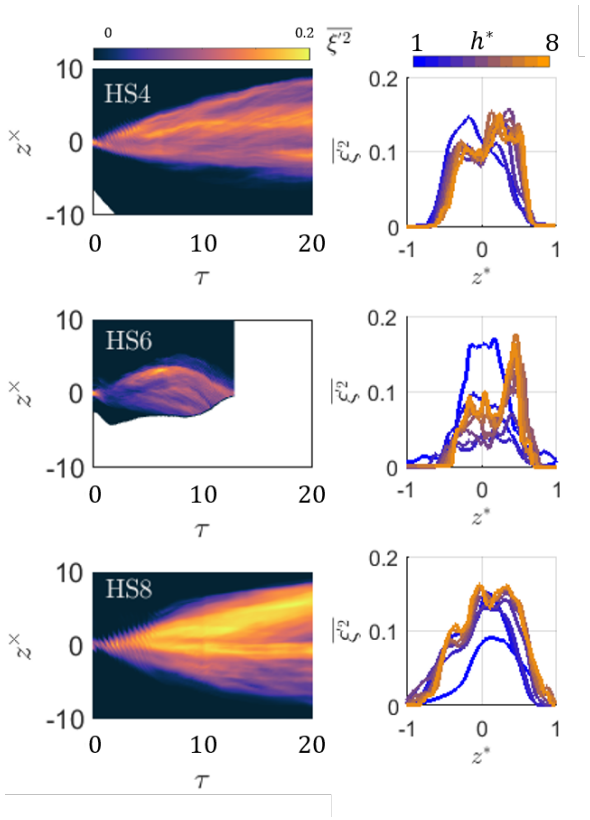

Figure 11: Left: contour plot of the spanwise variance of the light gas mole fraction $\overline{\xi'^2}$ in translating reference frame. Right: profiles of $\overline{\xi'^2}$ in the deforming reference frame.

asymmetry than HS4 and HS8.

A self-similarity analysis was performed by Ristorcelli *et al.* [25] on DNS data of a Rayleigh-Taylor unstable interface with an Atwood number of 0.01. Profile plots were normalised by the value at $z^* = 0$, and show similar trends initially. Asymmetries in the profiles, however, appear in the present case having a much higher Atwood number, compared to the persistent symmetry at the latest times shown by Ristorcelli *et al*.

Appendix C provides an argument for the physical interpretation of $\frac{\lambda}{\sqrt{hL}}$ as the effective turbulence bandwidth. This is plotted against the number of generations in Fig. 12 where $\hat{f} = \frac{1}{h}\int_{-\infty}^{\infty} f\, dz$ which is used to extract a single value for a given time similar to the process used by Schilling *et al.* [29]. Here $L = \frac{\int_{-\infty}^{\infty} k^{-1} E_\xi dk}{\int_{-\infty}^{\infty} E_\xi dk}$ is the integral scale where E_ξ is the spanwise scalar power spectrum. This plot shows that HS6 has access to a broader range of scales than HS4 and HS8. This aligns well with the initial Reynolds numbers for each experiment, such that a higher initial Reynolds number allows access to a broader range of scales.

This argument is furthered by looking at the normalised scalar dissipation C_χ, plotted in Fig. 13, where the profiles show a roughly constant value in space and time and the magnitude follows the same trend, with HS6 having the largest value and HS8 having the smallest so that large fluctuations are going to be more strongly damped in HS6.

Figure 14 is a plot of the time evolution of directional effective Taylor Reynolds numbers, whose form is derived in App. C. This is a measure of anisotropy, where the variance of gradients in an isotropic flow would not depend on the direction in which they are calculated. Here a relationship of $Re_{\lambda,x} = 1.2 Re_{\lambda,z}$ is seen a millisecond after the reflected shock has fully traversed the mixing layer in each of the experiments.

5.2. Skewness and Kurtosis of the Scalar Field

The skewness S_ξ and kurtosis K_ξ of the light-gas mole fraction spanwise distributions, defined in Eqs.(14 and 15), are shown in Fig. 15.

$$S_\xi = \frac{\mu_3}{\mu_2^{3/2}} \tag{14}$$

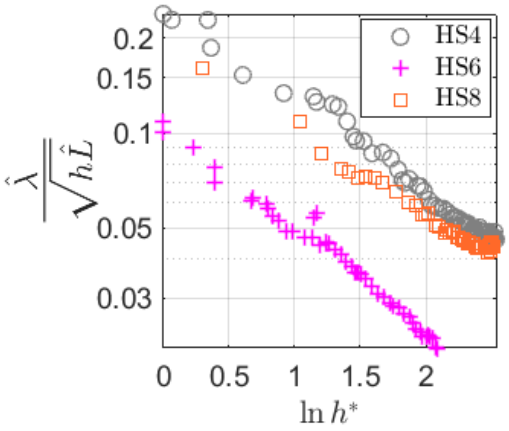

Figure 12: Effective turbulence bandwidth as a function of the number of generations.

$$K_\xi = \frac{\mu_4}{\mu_2^2} \tag{15}$$

$$\mu_n = \frac{1}{W}\int_0^W \xi'^n \, \mathrm{d}x \tag{16}$$

The skewness describes the asymmetry about the mean of a distribution. The kurtosis characterizes how prominent outliers or tails of the distribution are.

Schopflocher and Sullivan [30] studied the relationship between skewness and kurtosis for a passive diffusing scalar deriving relations of the form

$$S_\xi = \frac{\bar{\xi}(a_3 - 3a_2\bar{\xi} + 2\bar{\xi}^2)}{(\bar{\xi}(a_2 - \bar{\xi}))^{\frac{3}{2}}} \tag{17}$$

$$K_\xi = \frac{\bar{\xi}(a_4 - 4a_3\bar{\xi} + 6a_2\bar{\xi}^2 - 3\bar{\xi}^3)}{(\bar{\xi}(a_2 - \bar{\xi}))^2} \tag{18}$$

which leads to a parabolic relationship of the form

$$K_\xi = AS_\xi^2 + B \tag{19}$$

with the coefficients in general being time dependent. Here a_i are curve-fit parameters that allow the model to be fitted to experiment data. The dotted and dashed lines in Fig. 15 show Eq. (17) and (18) with $a_i = 1$ for all i, which corresponds to the naive PDF model not allowing

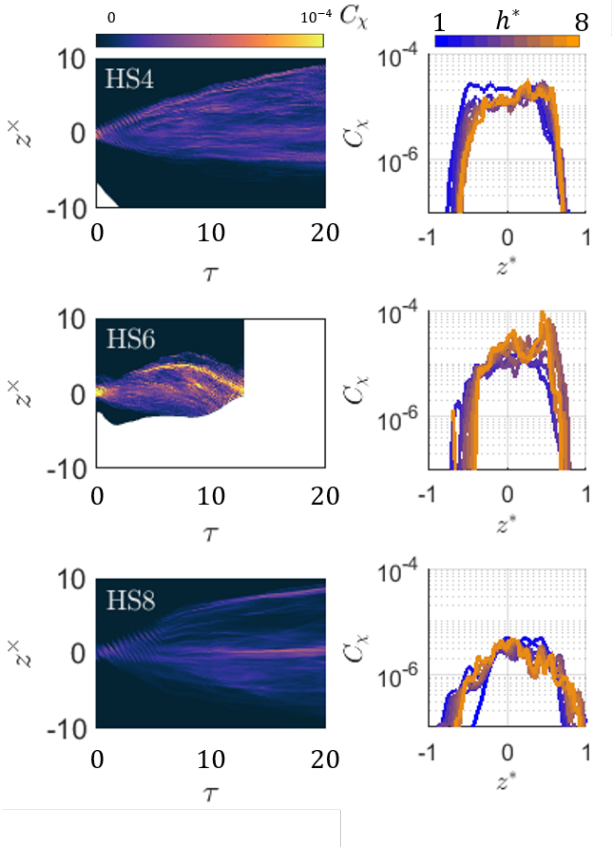

Figure 13: left: contour plot of the normalised scalar dissipation C_χ in translating reference frame, right: profiles of C_χ in the deforming reference frame.

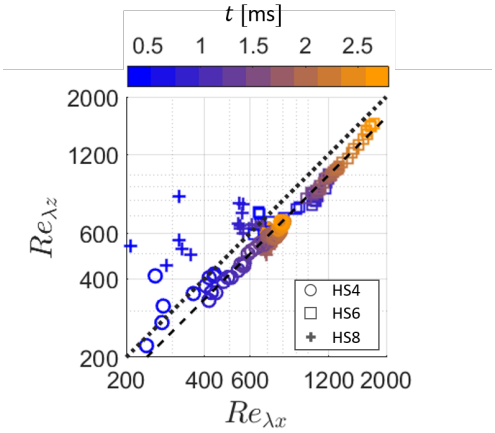

Figure 14: Anisotropy of the directional effective Taylor Reynolds numbers in log space. The dotted diagonal line represents isotropy. The dashed diagonal line represents $Re_{\lambda,x} = 1.2Re_{\lambda,z}$.

any fitting parameters derived by Schopflocher and Sullivan. Figure 16 shows the time variation of the A and B parameters. These are comparable to the values found in [30] from measurements conducted in a turbulent jet.

6. Conclusions

A set of experiments using high-speed PLIF were performed to investigate the Richtmyer-Meshkov instability upon re-shock.

The governing transport equation for the mole fraction was normalised to show that the number of generations appears as a natural measure of the dimensionless time in a mixing layer system.

A model for the growth rate of the mixing width was presented based on the deposition of vorticity not introducing any empirical fitting parameters. This was shown to overpredict the measured growth rate, while the Mikaelian model underpredicts it.

An analysis of the time evolution of spanwise averaged quantities was performed showing the appearance of asymmetry in moments of the light gas mole fraction spanwise distributions about the center of the mixing layer.

An inverse of an effective fluctuating bandwidth was defined and it was shown that this bandwidth grew the fastest for HS6 which had the highest initial outer-scale

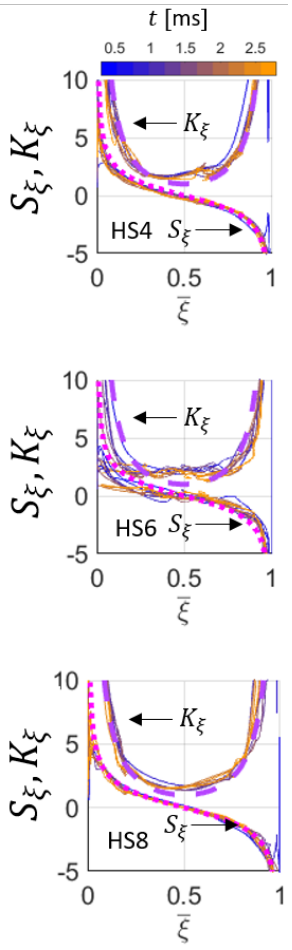

Figure 15: Plots of the spanwise skewness and kurtosis of the light gas mole fraction vs $\bar{\xi}$.(dashed line - Eq. (18), dotted line - Eq. (17)

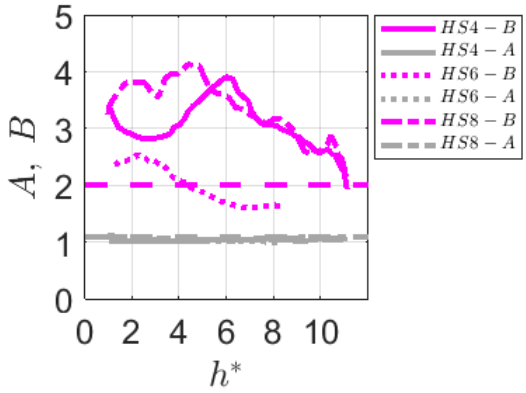

Figure 16: Evolution of curve fit parameters for the parabolic fit between kurtosis and skewness, Eq. (19). Dashed lines are representative values taken from Schopflocher and Sullivan [30].

Reynolds number of $7.8x10^4$. This shows that the flow in HS6 produced structures with a larger range of scales. Here the structure of the IC is seen to have a large effect: HS6 begins with a more diverse range of scales, and also contains the largest spanwise gradients which cause the largest deposition of velocity fluctuations leading to stronger shearing.

The anisotropy of the flow for the three highlighted experiments was shown to be a persistent, "frozen - in", anisotropy of $\sim$ 1.2 using the ratio of directional scalar-based Taylor scales. An effective Taylor Reynolds number of $Re_\lambda = 1800$ appears to have been reached before the reflected compression wave from the contact surface interacts with the mixing layer.

The skewness and kurtosis of the light gas mole fraction are presented and shown to follow previous results from turbulent jet experiments. A parabolic relationship between skewness and kurtosis and a rational relationship between skewness and kurtosis and the spanwise average light gas mole fraction were found to fit well.

7. Acknowledgments

This work is supported by the U.S. DOE/NNSA, through grant number DE-NA0002935.

Appendix A Derivation of governing equations

Using mass conservation

$$\frac{\partial \rho}{\partial t} + \boldsymbol{\nabla} \cdot \rho \boldsymbol{u} = 0, \tag{20}$$

Eq.(5) may be rewritten as

$$\frac{\partial \xi}{\partial t} + \boldsymbol{\nabla} \cdot \xi \boldsymbol{u} = \mathcal{D} \boldsymbol{\nabla}^2 \xi. \tag{21}$$

Then performing the transformation $\xi(t, x, z) \rightarrow \xi(h^*, x^*, z^*)$ where

$$\frac{\partial \xi}{\partial t} = \frac{\partial \xi}{\partial h^*}\frac{\partial h^*}{\partial t} + \frac{\partial \xi}{\partial z^*}\frac{\partial z^*}{\partial t} \tag{22}$$

$$\frac{\partial \xi}{\partial t} = \frac{\partial \xi}{\partial h^*}\frac{\dot{h}}{h_0} + \frac{\partial \xi}{\partial z^*}\Big(-\frac{V_0}{h} - z^*\frac{\dot{h}}{h}\Big), \tag{23}$$

the full transformed equation becomes

$$\frac{\partial \xi}{\partial h^*}\frac{\dot{h}}{h_0} + \frac{\partial \xi}{\partial z^*}\Big(-\frac{V_0}{h} - z^*\frac{\dot{h}}{h}\Big) + \frac{\partial \xi}{\partial z^*}\frac{V_0}{h} + \frac{\partial u^* \xi}{\partial x^*}\frac{\dot{h}}{L} + \frac{\partial w^* \xi}{\partial z^*}\frac{\dot{h}}{h} = \mathcal{D}\Big[\frac{\partial^2 \xi}{\partial x^{*2}}\Big(\frac{1}{L}\Big)^2 + \frac{\partial^2 \xi}{\partial z^{*2}}\Big(\frac{1}{h}\Big)^2\Big]. \tag{24}$$

Simplifying this leads to

$$\frac{\partial \xi}{\partial h^*}\frac{h}{h_0} - \frac{\partial \xi}{\partial z^*}z^* + \frac{\partial u^* \xi}{\partial x^*}\frac{h}{L} + \frac{\partial w^* \xi}{\partial z^*} = \frac{\mathcal{D}}{\dot{h}h}\Big[\frac{\partial^2 \xi}{\partial x^{*2}}\Big(\frac{h}{L}\Big)^2 + \frac{\partial^2 \xi}{\partial z^{*2}}\Big] \tag{25}$$

which is

$$\frac{\partial \xi}{\partial \ln h^*} - \frac{\partial \xi}{\partial z^*}z^* + \frac{\partial u^* \xi}{\partial x^*}\frac{h}{L} + \frac{\partial w^* \xi}{\partial z^*} = \frac{1}{Re_h Sc}\Big[\frac{\partial^2 \xi}{\partial x^{*2}}\Big(\frac{h}{L}\Big)^2 + \frac{\partial^2 \xi}{\partial z^{*2}}\Big] \tag{26}$$

Appendix B Derivation of post-shock growth rate estimate

Following Weber [28], the vorticity deposited by a planar shock wave is derived. Starting with the momentum equation

$$\frac{\partial \rho w}{\partial t} = -\frac{\partial p}{\partial z}. \tag{27}$$

Then the vorticity transport equation with only the baroclinic term is introduced

$$\frac{\partial \omega}{\partial t} = -\frac{1}{\rho^2}\frac{\partial p}{\partial z}\frac{\partial \rho}{\partial x} \tag{28}$$

which is

$$\frac{\partial \omega}{\partial t} = -\frac{1}{\rho^2}\frac{\partial \rho w}{\partial t}\frac{\partial \rho}{\partial x}. \tag{29}$$

Integrating over the interaction time leads to

$$\omega = -\frac{\Delta V_0}{\rho}\frac{\partial \rho}{\partial x} \tag{30}$$

which is

$$\frac{\partial w'}{\partial x} - \frac{\partial u'}{\partial z} = -\frac{\Delta V_0}{\rho}\frac{\partial \rho}{\partial x}. \tag{31}$$

If $w' >> u'$ then

$$\frac{w'}{\Delta V_0} = -(\ln \rho)' \tag{32}$$

which leads to an estimate of the initial growth rate after wave interaction of

$$\frac{\dot{h}_0}{\Delta V_0} = 8\int_{-\infty}^{\infty} \overline{(\ln \rho)' \xi'}\frac{\partial \overline{\xi}}{\partial z} dz - \frac{\dot{h}_{prs}}{\Delta V_0} \tag{33}$$

where $\dot{h}_{prs}$ is the pre-reshock mixing width growth rate.

Appendix C Physical interpretation of inhomogeneous Taylor scale

Here an argument is made for a physical interpretation of the scaled measured scalar-based Taylor scale as an estimate of the effective scalar power spectrum bandwidth.

We start from Eq.9 and choose a regime where the scalar variance is in steady state in the proposed non-dimensional coordinates, balancing orders of magnitude and proposing there is a balance between production and dissipation such that

$$\overline{w^* \xi'}\frac{\partial \overline{\xi}}{\partial z^*} = -\overline{\xi'^2}\frac{2}{\lambda_\xi^{*2}}\frac{1}{Re_h Sc}. \tag{34}$$

In this quasi-steady state, the mean mole fraction field can be approximated by $\bar{\xi} = \frac{1}{2} erfc(\frac{4z^*}{\sqrt{2\pi}})$ which leads to an approximation for $\overline{w^*\xi'}$

$$\overline{w^*\xi'} = -\frac{1}{4\sqrt{2}} \exp\Big(-\frac{8z^{*2}}{\pi}\Big). \tag{35}$$

Taking the centerline values leads to

$$\left(\frac{\lambda_0}{h}\right)^2 = 2\pi \frac{\overline{\xi'^2}_0}{Re_h Sc}. \tag{36}$$

Using the isotropic homogeneous relation between the integral scale, L, and the Taylor scale

$$\frac{1}{Re_h} = \frac{L}{h}\frac{1}{Re_L} = 10\frac{L}{h}\left(\frac{\lambda_{iso}}{L}\right)^2 \tag{37}$$

leads to

$$\frac{\lambda_0}{\sqrt{hL}} \propto \frac{\lambda_{iso}}{L} \tag{38}$$

such that $\frac{\lambda_0}{\sqrt{hL}}$ may be seen as an effective power spectrum bandwidth. Following this relation, the effective Taylor Reynolds number may be written as

$$Re_\lambda = \sqrt{\frac{3200}{3}}\frac{\sqrt{hL}}{\lambda_0} \tag{39}$$

Appendix D Error estimation

If $F = \left.\frac{\dot{h}_0}{\Delta V_0}\right|_{theory}$ from Eq. (33), then the uncertainty in F comes from three sources: an uncertainty in $\bar{\xi}$; in $\overline{\xi'^2}$; and in the Atwood number A. This can be written as

$$\delta F^2 = \left(\frac{\partial F}{\partial A}\delta A\right)^2 + \left(\frac{\partial F}{\partial \bar{\xi}}\delta\bar{\xi}\right)^2 + \left(\frac{\partial F}{\partial \overline{\xi'^2}}\delta\overline{\xi'^2}\right)^2. \tag{40}$$

The derivatives of F are approximated as

$$\frac{\partial F}{\partial A} = \frac{2.8}{A^2 - 1} \tag{41}$$

$$\frac{\partial F}{\partial \bar{\xi}} = 5.6\frac{A^2}{1-A} \tag{42}$$

$$\frac{\partial F}{\partial \overline{\xi'^2}} = 8\ln\frac{1+A}{1-A} \tag{43}$$

If $G = \left.\frac{\dot{h}_0}{\Delta V_0}\right|_{exp}$, then the uncertainty in G comes from two sources: an uncertainty in $\dot{h}$ and one in ΔV_0. This can be written as

$$\delta G^2 = \left(\frac{\partial G}{\partial \dot{h}}\delta\dot{h}\right)^2 + \left(\frac{\partial G}{\partial \Delta V_0}\delta\Delta V_0\right)^2 \tag{44}$$

δA is calculated by propagating error estimates through 1D gas dynamics equations. Uncertainties here arise from the measurement of the location of pressure transducers, which lead to uncertainties in the wave speeds and uncertainty in the rupture pressure of diaphragms. These lead to $\delta A = 0.04$.

The uncertainties in the light gas mole fraction field are estimated using regions of uniform gas such that $\delta\bar{\xi} = 0.014$ and $\delta\overline{\xi'^2} = 4.25E-04$

$\delta\dot{h}_0$ and $\delta\Delta V_0$ arise from uncertainties in the light gas mole fraction leading to $\delta\dot{h}_0 = 2.1$ and $\delta\Delta V_0 = 16$.

References

[1] J. D. Lindl, P. Amendt, R. L. Berger, S. G. Glendinning, S. H. Glenzer, S. W. Haan, R. L. Kauffman, O. L. Landen, L. J. Suter, The physics basis for ignition using indirect-drive targets on the National Ignition Facility, Physics of Plasmas 11 (2) (2004) 339–491. doi:10.1063/1.1578638.
URL http://aip.scitation.org/doi/10.1063/1.1578638

[2] F. E. Marble, G. J. Hendricks, E. E. Zukoski, Progress Toward Shock Enhancement of Supersonic Combustion Processes, Turbulent Reactive Flows 40 (1989) 26. doi:https://doi.org/10.1007/978-1-4613-9631-4_43.

[3] E. E. Meshkov, Instability of the interface of two gases accelerated by a shock wave, Fluid Dynamics 4 (5) (1972) 101–104. doi:10.1007/BF01015969.

URL http://link.springer.com/10.1007/BF01015969

[4] R. D. Richtmyer, Taylor instability in shock acceleration of compressible fluids, Communications on Pure and Applied Mathematics 13 (2) (1960) 297–319. doi:10.1002/cpa.3160130207.
URL http://doi.wiley.com/10.1002/cpa.3160130207

[5] M. Vetter, B. Sturtevant, Experiments on the richtmyer-meshkov instability of an air/sf6 interface, Shock Waves 4 (1995) 247–252.

[6] G. C. Orlicz, B. J. Balakumar, C. D. Tomkins, K. P. Prestridge, A Mach number study of the Richtmyer-Meshkov instability in a varicose, heavy-gas curtain, Physics of Fluids 21 (6) (2009) 064102. doi:10.1063/1.3147929.
URL http://aip.scitation.org/doi/10.1063/1.3147929

[7] M. A. Jones, J. W. Jacobs, A membraneless experiment for the study of Richtmyer-Meshkov instability of a shock-accelerated gas interface, Physics of Fluids 9 (10) (1997) 3078–3085. doi:10.1063/1.869416.
URL http://aip.scitation.org/doi/10.1063/1.869416

[8] C. Weber, B. Motl, J. Oakley, M. Anderson, R. Bonazza, Richtmyer-Meshkov Parameter Study, Fusion Science and Technology 56 (1) (2009) 460–464. doi:10.13182/FST09-A8945.
URL https://www.tandfonline.com/doi/full/10.13182/FST09-A8945

[9] V. V. Krivets, K. J. Ferguson, J. W. Jacobs, Turbulent mixing induced by richtmyer-meshkov instability, AIP Conference Proceedings 1793 (1) (2017) 150003. arXiv:https://aip.scitation.org/doi/pdf/10.1063/1.4971732, doi:10.1063/1.4971732.
URL https://aip.scitation.org/doi/abs/10.1063/1.4971732

[10] C. Weber, N. Haehn, J. Oakley, D. Rothamer, R. Bonazza, Turbulent mixing measurements in the Richtmyer-Meshkov instability, Physics of Fluids 24 (7) (2012) 074105. doi:10.1063/1.4733447.
URL http://aip.scitation.org/doi/10.1063/1.4733447

[11] J. A. McFarland, J. A. Greenough, D. Ranjan, Computational parametric study of a Richtmyer-Meshkov instability for an inclined interface, Physical Review E 84 (2) (2011) 026303. doi:10.1103/PhysRevE.84.026303.
URL https://link.aps.org/doi/10.1103/PhysRevE.84.026303

[12] K. Prestridge, P. M. Rightley, P. Vorobieff, R. F. Benjamin, N. A. Kurnit, Simultaneous density-field visualization and PIV of a shock-accelerated gas curtain, Experiments in Fluids 29 (4) (2000) 339–346. doi:10.1007/s003489900091.
URL http://link.springer.com/10.1007/s003489900091

[13] D. Reese, J. Oakley, A. Navarro-Nunez, D. Rothamer, C. Weber, R. Bonazza, Simultaneous concentration and velocity field measurements in a shock-accelerated mixing layer, Experiments in Fluids 55 (10) (2014) 1823. doi:10.1007/s00348-014-1823-4.
URL http://link.springer.com/10.1007/s00348-014-1823-4

[14] B. D. Collins, J. W. Jacobs, PLIF flow visualization and measurements of the Richtmyer-Meshkov instability of an air/SF6 interface, Journal of Fluid Mechanics 464. doi:10.1017/S0022112002008844.
URL http://www.journals.cambridge.org/abstract_S0022112002008844

[15] M. Mohaghar, J. Carter, B. Musci, D. Reilly, J. McFarland, D. Ranjan, Evaluation of turbulent mixing transition in a shock-driven variable-density flow, Journal of Fluid Mechanics; Cambridge 831 (2017) 779–825. doi:http://dx.doi.org/10.1017/jfm.2017.664.
URL https://search.proquest.com/docview/2007498246/abstract/61883C29F88048B0PQ/1

[16] M. Mohaghar, J. Carter, G. Pathikonda, D. Ranjan, The transition to turbulence in shock-driven mixing: effects of mach number and initial conditions 871 595–635. doi:10.1017/jfm.2019.330.
URL https://www.cambridge.org/core/product/identifier/S0022112019003306/type/journal_article

[17] J. Carter, G. Pathikonda, N. Jiang, J. J. Felver, S. Roy, D. Ranjan, Time-resolved measurements of turbulent mixing in shock-driven variable-density flows 9 (1) 20315. doi:10.1038/s41598-019-56736-w.
URL http://www.nature.com/articles/s41598-019-56736-w

[18] Y. Zhou, Rayleigh-Taylor and Richtmyer-Meshkov instability induced flow, turbulence, and mixing. I, Physics Reports 720-722 (2017) 1–136. doi:10.1016/j.physrep.2017.07.005.
URL http://www.sciencedirect.com/science/article/pii/S0370157317302028

[19] Y. Zhou, Rayleigh-Taylor and Richtmyer-Meshkov instability induced flow, turbulence, and mixing. II, Physics Reports 723-725 (2017) 1–160. doi:10.1016/j.physrep.2017.07.008.
URL http://www.sciencedirect.com/science/article/pii/S0370157317302958

[20] M. Anderson, B. Puranik, J. Oakley, P. Brooks, R. Bonazza, Shock tube investigation of hydrodynamic issues related to inertial confinement fusion, Shock Waves 10 (5) (2000) 377–387. doi:10.1007/s001930000067.
URL http://link.springer.com/10.1007/s001930000067

[21] C. Weber, N. Haehn, J. Oakley, D. Rothamer, R. Bonazza, An experimental investigation of the turbulent mixing transition in the Richtmyer-Meshkov instability, Journal of Fluid Mechanics 748 (2014) 457–487. doi:10.1017/jfm.2014.188.
URL http://www.journals.cambridge.org/abstract_S0022112014001888

[22] D. T. Reese, A. M. Ames, C. D. Noble, J. G. Oakley, D. A. Rothamer, R. Bonazza, Simultaneous direct measurements of concentration and velocity in the Richtmyer-Meshkov instability, Journal of Fluid Mechanics 849 (2018) 541–575. doi:10.1017/jfm.2018.419.

[23] J. M. Herzog, A. Ames, C. Noble, J. Oakley, R. Bonazza, D. A. Rothamer, Iterative correction of shocked acetone high-speed PLIF measurements in the Richtmyer-Meshkov instability, Proceedings of the International Symposium on Shock Waves 32 (2019) In Press.

[24] M. C. Thurber, F. Grisch, B. J. Kirby, M. Votsmeier, R. K. Hanson, Measurements and modeling of acetone laser-induced fluorescence with implications for temperature-imaging diagnostics, Applied Optics 37 (21) (1998) 4963. doi:10.1364/AO.37.004963.
URL https://www.osapublishing.org/abstract.cfm?URI=ao-37-21-4963

[25] J. R. Ristorcelli, T. T. Clark, Rayleigh-Taylor turbulence: self-similar analysis and direct numerical simulations, Journal of Fluid Mechanics 507 (2004) 213–253. doi:10.1017/S0022112004008286.
URL http://www.journals.cambridge.org/abstract_S0022112004008286

[26] B. E. Morgan, B. J. Olson, J. E. White, J. A. McFarland, Self-similarity of a Rayleigh-Taylor mixing layer at low Atwood number with a multimode initial perturbation, Journal of Turbulence 18 (10) (2017) 973–999. doi:10.1080/14685248.2017.1343477.
URL https://www.tandfonline.com/doi/full/10.1080/14685248.2017.1343477

[27] S. Ukai, K. Balakrishnan, S. Menon, Growth rate predictions of single- and multi-mode Richtmyer-Meshkov instability with reshock, Shock Waves 21 (6) (2011) 533–546. doi:10.1007/s00193-011-0332-0.
URL http://link.springer.com/10.1007/s00193-011-0332-0

[28] C. R. Weber, A. W. Cook, R. Bonazza, Growth rate of a shocked mixing layer with known initial perturbations, Journal of Fluid Mechanics 725 (2013) 372–401. doi:10.1017/jfm.2013.216.
URL http://www.journals.cambridge.org/abstract_S0022112013002164

[29] O. Schilling, M. Latini, W. S. Don, Physics of reshock and mixing in single-mode Richtmyer-Meshkov instability, Physical Review E 76 (2). doi:10.1103/PhysRevE.76.026319.
URL http://link.aps.org/doi/10.1103/PhysRevE.76.026319

[30] T. P. Schopflocher, P. J. Sullivan, The Relationship between Skewness and Kurtosis of A Diffusing Scalar, Boundary-Layer Meteorology 115 (3) (2005) 341–358. doi:10.1007/s10546-004-5642-7.
URL http://link.springer.com/10.1007/s10546-004-5642-7